

Photoexcited Carrier Dynamics in InAs, GaAs, and InSb Probed by Terahertz Excitation Spectroscopy

J. B. Héroux[†] and M. Kuwata-Gonokami^{*}

Department of Physics, The University of Tokyo, Tokyo 113-0033, Japan

(Received 18 December 2016; revised manuscript received 20 March 2017; published 5 May 2017)

The efficiency of terahertz emission by the photo-Dember effect from bare InAs, GaAs, and InSb samples as a function of the excitation-light wavelength is investigated to demonstrate that an electron-hole kinetic-energy equilibrium is rapidly reached, before the radiation peak. Numerical and experimental results show clear features that match the onset of electron scattering from the Γ valley to the L and X valleys. An ambipolar-based simulation model is developed to describe the above characteristics and to explain the experimental pump-fluence dependence of radiation emission from InAs. Results illustrate the potential of terahertz excitation spectroscopy to probe the electron density of states deep in the bands of semiconductor materials and obtain a depth profile of the dynamic forces acting on carriers at a subpicosecond time scale. Moreover, the potential of the further development of numerical models intrinsically including electron-hole attraction to describe photoinduced hot-carrier dynamics is explained.

DOI: 10.1103/PhysRevApplied.7.054001

I. INTRODUCTION

The collective motion of charge carriers having undergone a light-induced band-to-band transition in a semiconductor is a phenomenon that is at the heart of a wide range of critical technological uses and remains a very active research topic. The properties of hot electron-hole ensembles, about which much is still not precisely known, can be significantly different from the ones of intrinsic carriers, and alternative experimental methods have recently been employed for their characterization in a broad variety of materials. There is a need to better understand material performance limits on a short time scale in a high carrier energy and density environment.

One application example, within a very large body of literature, is the development of InP- and GaAs-based photodiodes for optical data receivers, where there is a trend towards smaller-area active regions with a micron-scale thickness to push data rates to 100 Gbit/s and beyond [1]. For high-speed and wide-spectral-band devices, high-energy electron scattering is a performance-limiting factor [2]. Another example involves the study of III-V semiconductor nanowires for high-sensitivity photodetection with possible nanoscale integration [3], with the GaAs/(Al, Ga)As material system with passivated surfaces being a candidate structure [4]. Finally, we mention polycrystalline silicon for low-cost solar-cell applications, where there is an interest in the improvement of nondestructive and quantitative characterization methods to reach better device performance [5].

While the fundamental analysis of materials with externally generated light pulses in the terahertz spectral range used as a pump or a probe beam is a rapidly growing research field to investigate carrier dynamics [6], another avenue that is particularly relevant in responding to the need for a contactless device evaluation method [7] is the detection and analysis of the terahertz radiation that is inherently emitted by carrier acceleration when a surface is excited by a femtosecond light pulse with a photon energy larger than the semiconductor band gap. This phenomenon occurs for a wide variety of material systems, including the three examples given above, namely, III-V p - i - n structures [8], GaAs/(Al, Ga)As quantum wires [9], and polysilicon layers [10]. Compared to more well-known femtosecond optical characterization tools, this technique has some advantages. In dynamic photoluminescence spectroscopy, the signal comes from carriers undergoing a band-to-band recombination and is related to the product of the electron and hole carrier densities. In ultrafast pump-probe measurements, the probe interaction with the sample may also involve a band-to-band transition; a significant spatial mismatch with the excited carriers may occur if the two light pulses have different wavelengths, decreasing sensitivity and attainable resolution. Terahertz emission, by contrast, is a naturally occurring process that is a signature unique to the carriers during their flight time before they recombine. It has the potential to provide, for a given material and excitation wavelength, a complete physical picture and precise spatial profile of the dynamic forces acting on carriers at a subpicosecond time scale in the direction perpendicular to the surface.

When photons having an energy above the band gap are efficiently absorbed as a result of the illumination of a finite semiconductor surface, the diffusion forces acting on the

^{*}Corresponding author.

gonokami@phys.s.u-tokyo.ac.jp

[†]Present address: IBM Research–Tokyo, Shin-Kawasaki 7-7, Kawasaki, Kanagawa 212-0032, Japan.

generated electron and hole ensembles are unequal. Therefore, an electric-field distribution in the material is created, a phenomenon that was discovered over 80 yr ago called the photo-Dember effect [11]. If the excitation is a short light pulse, the so-called Dember field may reach a large amplitude and a current surge is produced in the sample. This mechanism, along with the possible influence of a built-in electric field due to a band-bending effect, is responsible for the emission of terahertz radiation from semiconductor surfaces via carrier acceleration [12]. The experimental investigation of this process in the previous two decades has been extensive, driven by the technological need for a good source in this spectral range. The efficiency dependence on a variety of factors, such as applied electric and magnetic fields, the sample background carrier type and concentration, excitation wavelength, temperature, and crystal orientation, has been studied [13–19].

Two schemes have been recently proposed for the goal of using terahertz emission specifically, instead, for material characterization. In terahertz excitation spectroscopy [20–22], the wavelength of the pump pulse is scanned over a given range under otherwise-unchanged measurement conditions and terahertz spectra are recorded at a number of steps to gain some insight on a semiconductor band structure, particularly the upper conduction valleys. Second, with laser terahertz emission microscopy [23], a micron-scale surface spatial resolution is attainable with specially designed optics. Carrier dynamics in mono- and polycrystals has been evaluated, with demonstrated advantages in terms of richness of information and defect sensitivity over other evaluation methods for photovoltaics [24,25].

Despite these developments, the full possibilities of terahertz emission for the study of carrier dynamics, which is the topic of this work, have not been reached so far—even for homogeneous materials—for a few reasons. For certain crystalline orientations, a coherent nonlinear difference frequency terahertz radiation mechanism may dominate over the effect of carrier acceleration, complicating analysis. Moreover, if the band gap is relatively large and there is band bending at the surface, electrons and holes may accelerate in opposite directions due to the built-in field, unlike for a diffusion effect in flatband conditions [12]. Another important obstacle may be that, even though the photo-Dember effect is a well-known phenomenon, no simulation environment that gives a complete picture of experimental results has been described thus far, limiting measurement interpretation.

The most common formalism to simulate terahertz emission is a semiclassical drift-diffusion model in which the time-dependent photoexcited hole and electron carrier densities are calculated as separate entities, and Coulomb attraction is taken into account at small time steps with the Poisson equation in a quasistatic approximation. A good understanding of the influence of an electric field on the waveform and of the terahertz-radiation enhancement with the application of a magnetic field due to dipole rotation has

been reached with this framework [26,27]. While a number of numerical studies have been published that elucidate the effect of other parameters such as sample doping, band structure, material, and optical-pulse length [28–33], detailed comparisons between calculated and experimental results have been scarce. In particular, a model describing the efficiency for a given material in the two-dimensional space formed by photon energy and density, which may be the most basic experimental parameters involved and are critical for terahertz excitation spectroscopy, has yet to be demonstrated.

In most numerical analyses, a Monte Carlo method adapted from a formalism originally developed for unipolar devices (see, e.g., Ref. [34]) has been used to treat carrier drift and diffusion by including several scattering mechanisms. A technical difficulty may then arise due to the physical quantities involved in the material. For example, in InAs, a typical energy per pulse of the order of 1 μJ with an 800-nm center wavelength and a spot size of around 1 mm results in a surface carrier density above 10^{19} cm^{-3} . Assuming a realistic Dember voltage (the spatial depth integral of the photoinduced Dember field) of the order of 1 V, this energy per pulse would correspond to an electron-hole difference ratio in the material in the vicinity of 10^{-4} . An accurate calculation at a given time step of the quasistatic field *a priori* with Poisson's equation in these typical conditions would require a simulated precision of at least four digits for the electron and hole spatial distributions, a nontrivial task even in a one-dimensional approximation for a method relying on repeated random sampling of electrons and holes. The usual Monte Carlo methods are not ideally suited to this problem.

In this work, we perform a detailed numerical and experimental analysis of the terahertz emission efficiency of three common homogeneous semiconductors, bare InAs, GaAs, and InSb surfaces, over a broad range of excitation wavelengths, in an attempt to provide a stronger basis to reach the full potential of this phenomenon for carrier-dynamics characterization purposes and then apply it to other materials. The experimental conditions are designed to isolate the photo-Dember effect and minimize other emission mechanisms, with an optical excitation power below saturation, but strong enough to give a clear signal. The ambipolar-based, finite-difference model that we developed allows us to successfully reproduce experimental results by adjusting, to realistic values, only the electron effective masses in the L and X valleys and using established data without any tuning for other band parameters. We purposely avoid including any variable that has no large influence on the results, in an attempt to keep the calculation as simple as possible. We find clear features that match the onset of scattering mechanisms involving the L and X valleys assuming an electron-hole equilibrium process that is faster than the radiation emission peak, and we gain some insight on the carrier dynamics in a high-injection regime. In a previous study, we developed an ambipolar simulation to describe, on a picosecond and longer time scale, the properties of the magnetic semiconductor (Ga,Mn)As under pulsed

excitation with the concept of electron, lattice, and spin temperature reservoirs [35]. The model that we use here is related, being an extension to a faster process in which we can assume that the carrier and lattice temperatures remain constant and that there is no spin effect.

II. EXPERIMENTAL DETAILS

The three single-crystal samples that are used for the measurements are commercially available from Furuichi Chemical Inc. and are chosen for this photo-Dember study: they are nonintentionally doped [an n -type residual carrier concentration below $5 \times 10^{16} \text{ cm}^{-3}$] with a (100) surface orientation and are polished for epitaxial growth. The samples are rotated to eliminate the coherent nonlinear process component of the terahertz signal, which is, in any case, only a few percent for this crystal orientation [12].

The reflection-configuration terahertz characterization setup is a standard one with electro-optical sampling detection using a ZnTe detector crystal, two parabolic mirrors, a Wollaston prism, a balanced high-speed photo-detector, and a lock-in amplifier.

The linearly polarized master light pulses are provided by a Ti:sapphire laser with a 1-kHz repetition rate, a 150-fs temporal width, and an 800-nm wavelength. They are split into a small fraction reaching the ZnTe crystal, and a larger part that entered a commercially available optical-parametric-amplifier system with a tunable range from 470 to 1600 nm. For the optical parametric generation, a type-II phase-matched β -barium borate crystal is used to generate colinearly propagating signal and idler beams. The desired output wavelength is obtained from standard coherent nonlinear optical processes and dichroic filters. The excitation power reaching the sample is adjusted with a neutral-density filter, and the beam is slightly focused to get a 1-mm-diameter excitation spot size with a 45° incidence angle. For each excitation wavelength, the power is adjusted to maintain a nearly constant 3×10^{12} number of photons per pulse, which corresponds to a $1.65 \mu\text{J}$ energy per pulse at 800 nm. The experimental data are analyzed to confirm that the measured features are not correlated with specific coherent nonlinear processes of the excitation pulse.

III. NUMERICAL MODEL

The equation set that we apply for result analysis is based on the work of Hwang and Lindholm [36,37], who studied the static and time-dependent Dember effect in photoconductive detectors three decades ago. The key approximation that is made throughout is to neglect the difference between the photogenerated electron and hole densities. As photons are incident at 45° outside the sample, the propagation angle inside the sample determined by Snell's law is small [38]. We neglect this angle and assume a single dimension perpendicular to the surface. The one-dimensional carrier distribution is given by a standard ambipolar equation,

$$\frac{dn}{dt} \approx \frac{dp}{dt} = G_0 e^{-\alpha z} + \frac{1}{q} \frac{\partial j_a}{\partial z} - \frac{n}{\tau_{\text{rec}}}, \quad (1)$$

where n and p are the electron and hole concentrations, G_0 is a photon-generation function that can be time dependent, α is the light absorption coefficient, and τ_{rec} is a carrier recombination time. Surface recombination and reflection and band-bending effects leading to a built-in field are neglected. The ambipolar current j_a has four components, electron diffusion j_{nD} , electron conduction j_{nE} , hole diffusion j_{pD} , and hole conduction j_{pE} . It is given by

$$\begin{aligned} j_a &= j_n + j_p \\ j_n &= j_{nD} + j_{nE} = qD_n \frac{\partial n}{\partial z} + q\mu_n n E_D \\ j_p &= j_{pD} + j_{pE} = -qD_p \frac{\partial p}{\partial z} + q\mu_p p E_D \\ n &= n_0 + \Delta n \\ p &= p_0 + \Delta p, \end{aligned} \quad (2)$$

where j_n and j_p are the total electron and hole current densities, n_0 , p_0 , and Δn , Δp are the background and photogenerated electron and hole carrier densities, respectively, D_n , D_p , and μ_n , μ_p are the electron and hole diffusion coefficients and mobilities, respectively, and E_D is the Dember field due to the incoming light-generating carriers.

For the case of a steady-state excitation, we have $j_a = 0$, and E_D can be easily calculated from Eq. (2). Defining, following common textbook notation, $b = \mu_n/\mu_p$, $\sigma_0 = q(\mu_n n_0 + \mu_p p_0)$, and $D_n = kT_n \mu_n/q$, $D_p = kT_p \mu_p/q$, we obtain

$$\begin{aligned} E_D &= \frac{q(D_p - D_n)\partial\Delta p/\partial z}{\sigma_0 + q(\mu_n + \mu_p)\Delta p} \\ &= \frac{kT}{q} \frac{b-1}{b+1} \left(\frac{(b+1)\partial\Delta p/\partial z}{p_0 + bn_0 + (b+1)\Delta p} \right), \end{aligned} \quad (3)$$

where the electrons and holes have the same carrier temperature, $T = T_n = T_p$. The part in parentheses on the right-hand side can be integrated analytically to obtain the well-known expression for the steady-state Dember voltage [39]

$$V_D = - \int E_D dz = \frac{-kT}{q} \frac{b-1}{b+1} \ln \left(1 + \frac{(b+1)\Delta p}{p_0 + bn_0} \right) \quad (4)$$

that provides a convenient rule of thumb for recognizing the important parameters of the Dember effect, particularly the mobility ratio b and the carrier temperature depending on the excitation-light wavelength.

For a pulsed excitation with a high injection condition, $n \approx p \gg n_0, p_0$, the displacement current $\epsilon \partial E_D / \partial t$ must be included following Maxwell's time-dependent equations and the total current j_{tot} is

$$j_{\text{tot}} = j_a + j_{\text{disp}} = qD_a \nabla n + q\mu_a E_D + \frac{\epsilon \partial E_D}{\partial t} = 0, \quad (5)$$

where ϵ is the dielectric permittivity and the ambipolar diffusion coefficient and mobility D_a and μ_a are given as [37]

$$D_a = \frac{p+n}{p/D_n + n/D_p} \approx \frac{2}{1/D_n + 1/D_p}$$

$$\mu_a = \frac{p-n}{p/\mu_n + n/\mu_p} \approx 0, \quad (6)$$

where the electron and hole carrier temperatures modifying the diffusion coefficients may be different.

In the time scale of interest, we neglect carrier recombination and the variation of the average carrier energy (temperature). At a time t_i , the carrier distribution n can be calculated from Eq. (1). By numerical integration, the Dember field E_D is obtained from Eq. (5) to compute the current component inputs at the next time step (5 attosecond interval).

The terahertz radiation is calculated from the usual equations related to the dipole moment $p(t)$ with an area S in a quasi-one-dimensional approximation at a fixed distance far from the sample:

$$\frac{dp(t)}{dt} \propto S \int (j_n + j_p) dz (Am)$$

$$E_{\text{THz}} \propto \frac{d^2 p}{dt^2} \left(\frac{Am}{s} \right). \quad (7)$$

In this work, the photon excitation energy is varied over a broad range in samples having a large disparity in their band-gap values. Charge carriers are typically excited deep in the bands, and this fact must be taken into account. For the holes, at a high energy, the heavy and light valence bands generally become parallel [40] and band mixing occurs, possibly including the split-off band. For this analysis, we use a single, parabolic valence band approximation with a heavy-hole mass for this complex structure, as the terahertz emission is not critically sensitive to the hole carrier motion.

For the electrons, the population distribution evolution in the Γ , L , and X valleys must be taken into account. The kinetic energies in band i , kT_i are given by the relations

$$kT_\Gamma = f(\hbar\omega - E_G)$$

$$kT_L = kT_\Gamma - \Delta E_{L\Gamma}$$

$$kT_X = kT_\Gamma - \Delta E_{X\Gamma}$$

$$kT_{HH} = (1-f)(\hbar\omega - E_G), \quad (8)$$

where $\hbar\omega$ is the photon energy, E_G the room-temperature-material band gap, $\Delta E_{L\Gamma}$ ($\Delta E_{X\Gamma}$) is the energy difference between the bottom of the L (X) band and the Γ band, and f is the fraction of the total kinetic energy going to the electrons, while $(1-f)$ is the energy fraction of the holes in the valence band HH .

We assume that the electrons are initially generated in the Γ band and use a linear interpolation equation set,

$$n = n_\Gamma + n_L + n_X$$

$$\frac{dn}{dt} = \frac{dn_\Gamma}{dt} + \frac{dn_L}{dt} + \frac{dn_X}{dt}$$

$$\frac{dn_\Gamma}{dt} = \frac{-n_\Gamma}{\tau_{\Gamma L}} + \frac{n_L}{\tau_{L\Gamma}} + \frac{-n_\Gamma}{\tau_{\Gamma X}} + \frac{n_X}{\tau_{X\Gamma}} + G_0 e^{-\alpha z} + \frac{1}{q} \frac{n_\Gamma}{n} \nabla j_a$$

$$\frac{dn_L}{dt} = \frac{-n_L}{\tau_{L\Gamma}} + \frac{n_\Gamma}{\tau_{\Gamma L}} + \frac{-n_L}{\tau_{LX}} + \frac{n_X}{\tau_{XL}} + \frac{1}{q} \frac{n_L}{n} \nabla j_a$$

$$\frac{dn_X}{dt} = \frac{-n_X}{\tau_{X\Gamma}} + \frac{n_\Gamma}{\tau_{\Gamma X}} + \frac{-n_X}{\tau_{XL}} + \frac{n_L}{\tau_{LX}} + \frac{1}{q} \frac{n_X}{n} \nabla j_a, \quad (9)$$

where n_Γ , n_L , and n_X are the position-dependent band populations.

The intervalley transition rates from band i to band j , $W_{ij}(E_i) = 1/\tau_{ij}$, are due to nonpolar optical-phonon scattering and are critical for determining the effect of the L and X valleys on the terahertz signal. They are given by the well-known expression [34]

$$W_{ij}(E_i) = \frac{\pi D_{ij}^2}{\rho \omega_{ij}} [n(\omega_{ij}) + 1/2 \mp 1/2] N_j(E_i \pm \hbar\omega_{ij} - \Delta E_{ji})$$

$$N_j(E) = \frac{\sqrt{2m_j^*{}^3 E}}{2\pi^2 \hbar^3}, \quad (10)$$

where E_i is the carrier kinetic energy in band i [Eq. (8)], ΔE_{ji} is the energy difference between bands j and i , and $\hbar\omega_{ij}$ is the phonon energy, with the plus and minus corresponding to absorption and emission, respectively, while D_{ij} , ρ , and $n(\omega_{ij})$ are the deformation potential, the material density, and the phonon mode number, respectively. $N_j(E)$ is the density of states in band j to which the carrier is scattered, with m_j^* being the effective mass.

The electron mobility and the diffusion coefficient, μ_n and D_n , also depend on band population and are linearly interpolated, even though, in practice, the Γ components are much larger and primarily determine the terahertz-radiation emission strength:

$$\mu_n = \frac{n_\Gamma}{n} \mu_\Gamma + \frac{n_L}{n} \mu_L + \frac{n_X}{n} \mu_X \quad (11)$$

$$D_n = \frac{n_\Gamma}{n} D_\Gamma + \frac{n_L}{n} D_L + \frac{n_X}{n} D_X. \quad (12)$$

For the hot-carrier mobility and diffusion in each band, we follow the theory described by Lundstrom [41] assuming Matthiessen's rule. The mobility in band i is given by

$$\mu_i = \frac{q \langle \tau_{mi} \rangle}{m_i^*}, \quad (13)$$

where $\langle \tau_{mi} \rangle$ is the energy-dependent momentum relaxation time and includes optical and acoustic phonon and impurity scattering. Nonpolar optical phonon scattering is isotropic, so that the collision time obtained from Eq. (10) is equal to

TABLE I. Material band parameters at room temperature used in the calculations.

Parameter	Band	E_{gap} (eV)	$m^*(m_0)$	$\alpha(\text{eV}^{-1})$
InAs	Γ	0.354	0.026	1.4
	L	1.07	0.1 ^a	0.76
	X	1.370	0.2 ^a	0.47
	HH	...	0.41	0
GaAs	Γ	1.42	0.067	0.61
	L	1.704	0.2 ^a	0.37
	X	1.896	0.8	0.02
	HH	...	0.51	0
InSb	Γ	0.240	0.0135	4.1
	L	0.935	0.09 ^a	0.87
	X	0.635	0.1 ^a	1.28
	HH	...	0.43	0

^aValue adjusted according to experimental results.

the momentum relaxation time for this process. The diffusion coefficients are given as

$$D_i = \frac{2u_{zi}\mu_i}{q} = \langle v_{zi}^2 \tau_{mi} \rangle, \quad (14)$$

where u_{zi} and v_{zi} are the average kinetic energy and velocity, respectively, associated with the degree of freedom oriented along the diffusion-direction axis z , approximately perpendicular to the surface.

With the formalism described, all important parameters for terahertz radiation are taken into account, while noncritical factors are kept to their most simple form. Table I shows the band-structure values used for the analysis and simulations. All values related to the Γ and heavy-hole bands, as well as the energy positions of the L and X conduction valley bottom, are well established [42,43] and kept unchanged. We allow for some variation in the effective masses of the L and X valleys, with the nonparabolicity factors calculated with a $k \cdot p$ model.

The wavelength-dependent complex refractive indices are also standard values [44]. The dielectric permittivity is calculated from the usual static and high-frequency values as $\epsilon = 1/[\epsilon(0)^{-1} + \epsilon(\infty)^{-1}]$. The phonon and impurity scattering-parameter values are taken from Ref. [45] for InAs and GaAs, and from Ref. [46] for InSb, with a 10^{15} cm^{-3} impurity level. The hole optical deformation potential is set equal to the interband Γ - L value.

IV. RESULTS AND DISCUSSION

A. InAs analysis

For the InAs sample that gave the best signal-to-noise ratio, measurements are taken for the entire range of available photon energies. Figure 1(a) shows an enlarged view of the experimental and simulated curves at 1.65 eV, which is near the condition for which the terahertz signal is the strongest. Three main features are seen in the time-resolved spectra that we measure: a first dip, which we do not attempt to simulate or investigate in this work and

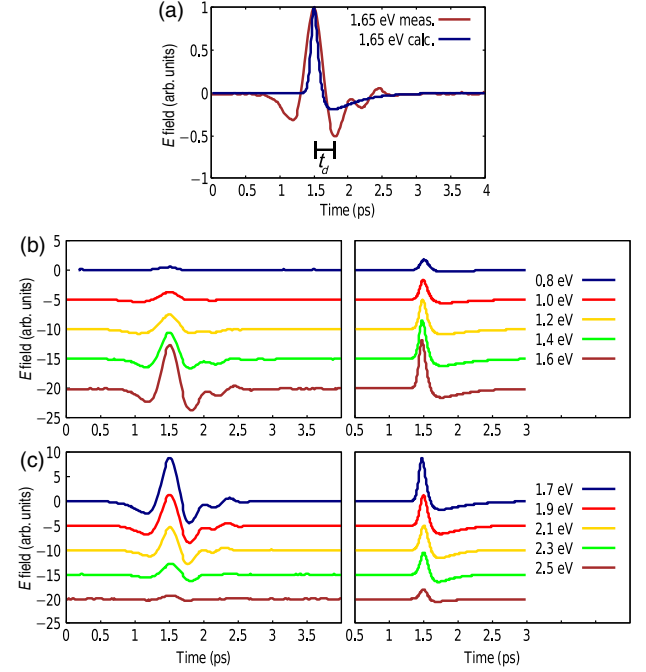


FIG. 1. (a) Overlapped experimental and simulated InAs terahertz emission curves in the time domain at 1.65 eV, i.e., in the vicinity of the maximum signal. (b) Experimental (left panel) and simulated (right panel) terahertz emission curves for a signal strength that increases with the photon energy. (c) Experimental (left panel) and simulated (right panel) terahertz emission curves for a signal strength that decreases with the photon energy. Electron-hole energy equilibrium is assumed for the calculations. The horizontal position of the curves is adjusted to obtain a peak at 1.5 ps.

which could be attributed to a detection artifact, initial carrier reflection off the surface, band bending, or some other phenomenon; the main peak, associated with electron acceleration; and a valley following the main peak that is related to electron deceleration. A single-pole low-pass frequency filter, equivalent to a convolution process in the time domain, is applied to the raw curve obtained with the equation set of the previous section to take into account broadening due to the electro-optical detection system and other experimental factors. Good agreement for the relative positions of the main peak and the following valley is found with a 1.7-ps filter time constant, and we keep this value unchanged for all calculations.

The goal of the analysis is not to reproduce precisely the shape of the measured curve, as the model is too basic for this task, but rather to gain an understanding of the variation of emission characteristics as a function of the pump-beam properties. The left-hand panels of Figs. 1(b) and 1(c) show, on a fixed vertical-axis scale, measured terahertz signal curves in the time domain at various pump energies. While we observe a clear amplitude variation, the shape of the spectra corresponding to a peak in the vicinity of 1 THz in the frequency domain remains nearly unchanged.

Owing to this fact, the amplitude of the main peak is representative of the overall emission strength and is also an experimentally stable feature with low sensitivity to noise or broadening-effect variations. Our primary goal is to quantitatively reproduce this amplitude variation, and the right-hand panels of Figs. 1(b) and 1(c) show that the shape of the simulated curves, with a time delay between the main peak and the following valley $t_d = 0.3$ ps, is also very stable, in good agreement with the measurements. One can also observe that the depth of the secondary valley is maximized around 1.7–2.1 eV in both the experimental and the simulated curve, indicating a stronger deceleration mechanism as the signal strength starts to decrease with the increasing pump photon energy. At a higher energy range, the acceleration of carriers is progressively inhibited.

In Fig. 2(a), we plot the experimental values of the maximum signal amplitude as a function of the photon excitation energy, and a clear maximum is observed at 1.7 eV, in good agreement with previously published data [20]. At a lower energy, a linear shape is measured as

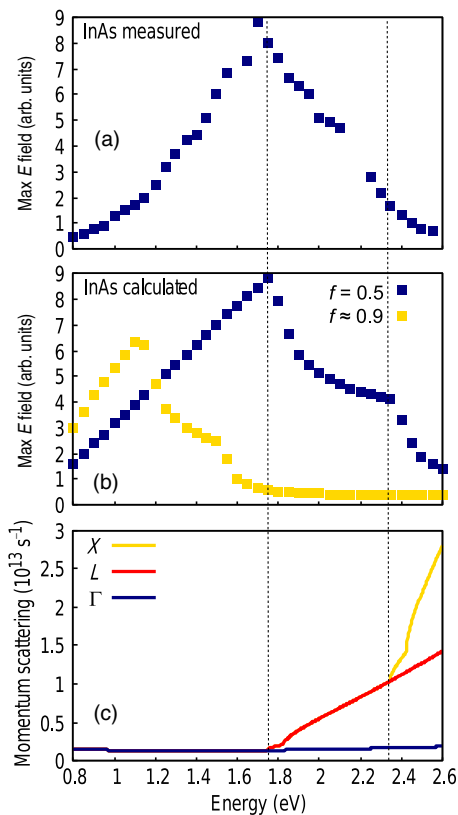


FIG. 2. (a) Plot of the experimental maximum time-domain terahertz signal amplitude for InAs as a function of the photon energy. (b) Simulated result with equal hole and Γ electron kinetic energy (blue) and equal momentum (yellow). (c) Calculated Γ -band scattering rate for equal kinetic energy. The legend refers to the band to which carriers are scattered. The dashed lines positioned at the phonon-absorption thresholds show the alignment of features in (a), (b), and (c).

expected, as the diffusion coefficients vary proportionally with the carrier temperature. Above the maximum, we observe a decrease that is also linear and is attributed to the effect of the L and X valleys.

The first parameter that must be determined to analyze results is the fraction f of the total photon energy that goes to the electrons, as the position of the peak is very sensitive to this value. Three possibilities are investigated. First, as electron-hole pairs are initially generated with equal momentum ($p = \hbar k$), is the case in which there is negligible electron-hole heat exchange, as equilibrium is typically reached in a picosecond time scale [47]. This situation would correspond to $f \approx 0.9$, based on the Γ electron and hole effective masses. The second and third cases are for partial and complete energy exchanges, $0.5 < f < 0.9$ and $f = 0.5$, respectively. Figure 2(b) shows curves for $f \approx 0.9$ (yellow) and $f = 0.5$ (blue). A large difference in the peak position is found, and the latter curve clearly matches the experimental results, indicating that electron-hole energy redistribution occurs on a shorter time scale than the terahertz peak amplitude.

The second adjusted parameter involves the electron effective masses in the L and X valleys. Carriers in these bands have a low velocity and do not contribute to the radiation emission; however, the densities of states depending on the masses will affect the electron population as well as the momentum scattering time in the Γ band [Eq. (10)]. A value $m_L = 0.1m_0$ gives an excellent match to the experimental results, with a nonparabolicity factor calculated from a $k \cdot p$ model. In the 2.4–2.6 eV range, scattering to the X valley occurs and $m_X = 0.2m_0$ is used; a higher value around $m_X = 0.6m_0$ would completely turn off the emission. Overall, remarkably good agreement is reached, considering the simplicity of the calculation and also that no adjustment of the valley energy positions is performed. m_L and m_X are within the established values for the longitudinal and transversal masses [42]. The symmetry of the curves in Figs. 2(a) and 2(b) is also very similar, with comparable signal strengths near 0.8 and 2.6 eV.

Figure 2(c) shows the calculated Γ -band momentum scattering with $f = 0.5$. Below the emission peak, the rate varies little and the dominant mechanism is polar-optical-phonon scattering. The radiation signal variation can be attributed to the change of the carrier velocity affecting the diffusion coefficient [Eq. (14)]. After the onset of intervalley scattering via phonon emission and absorption [Eq. (10)], the decrease in τ_m in the Γ band becomes significant and the diffusion coefficient decreases.

In Fig. 3, we attempt to give a sense of the physical values within the sample involved in the calculations, and in Fig. 3(a) is shown the relative carrier-population time evolution in each of the conduction bands at specific excitation photon energies calculated from Eqs. (9) and (10). As expected, the decrease of the Γ -electron population is not perfectly correlated with the emission strength—as, for

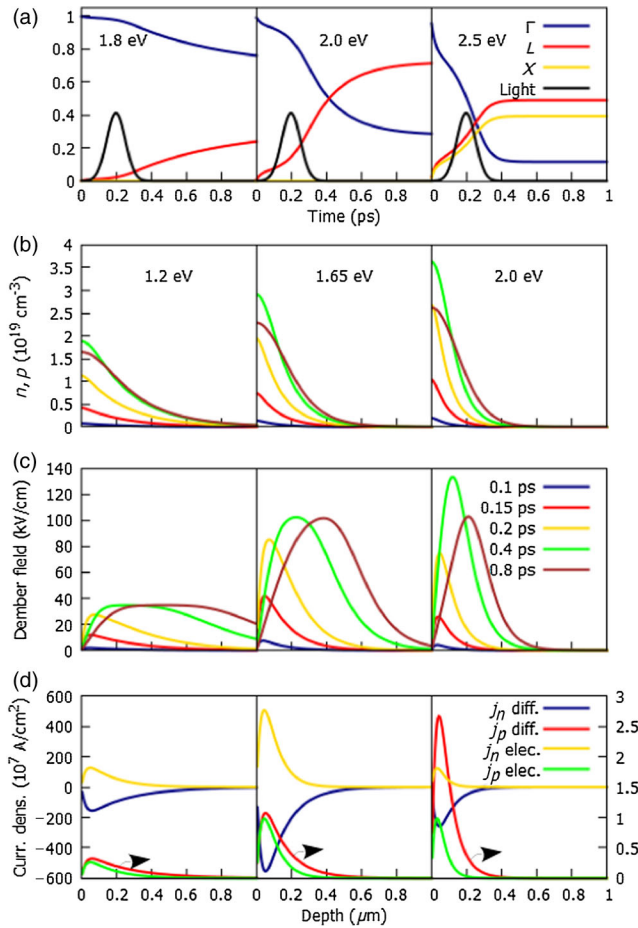


FIG. 3. (a) Calculated time evolution of the band population fraction for the 1.8-eV (left panel), 2.0-eV (center panel), and 2.5-eV (right panel) photon energies in InAs. The black lines show the excitation pulse on an arbitrary scale centered at 0.2 ps. (b) Electron and hole carrier concentration profiles for 1.2, 1.65, and 2.0 eV photon excitation energies in InAs. (c) Calculated Dember-field profile. (d) Hole and electron diffusion and conduction-current components [Eq. (2)] at the peak of the optical excitation (0.2 ps).

example, at 2.5 eV approximately 50% of the carriers are in the upper valley near the exciting-pulse maximum, but the terahertz signal in Fig. 2(a) is nearly extinct due to the short Γ -electron scattering time.

The time-dependent carrier-density profiles at the 1.2, 1.65, and 2.0 eV pump energies are shown in Fig. 3(b) and are determined by the absorption depth and the ambipolar diffusion coefficient in the material. These photon energy values are chosen to illustrate low absorption and carrier kinetic energy, strong terahertz emission and strong inter-band scattering regimes, respectively. At 2.0 eV, the higher photon-absorption coefficient and the electron scattering to the L and X valleys tend to decrease carrier penetration in the sample; however, these effects are balanced by the higher kinetic energy of the holes promoting the ambipolar diffusion. As a result, the profile changes little compared to

1.65 eV. The Dember field calculated from Eq. (5) is shown in Fig. 3(c). For time delays longer than the exciting pulse (0.4 and 0.8 ps) or deep in the sample, the calculation may somewhat overestimate the field strength, as carrier recombination, energy relaxation, electron-hole concentration difference, and background carrier effects are not taken into account. However, the general mechanisms involved are correctly described. At 2.0 eV and 0.2 ps, the maximum field strength does not decrease much, but the Dember voltage is lower than it is at 1.65 eV.

The four calculated current components at the peak photon excitation time are shown in Fig. 3(d). The negative electron diffusion current always dominates, but a large fraction is balanced by the electron conduction current. For the holes, the diffusion and conduction components have the same polarity and are 2 orders of magnitude smaller. They increase monotonically with the exciting-photon energy in this single-valence-band model. Overall, while some of the quantitative values shown in Fig. 3 may be approximate, a convincing physical picture is reached.

A first consistency check of our analysis comes from an examination of the variation of the terahertz emission peak amplitude with the optical power—i.e., the number of photons per pulse at a given wavelength—that has often been plotted using linear-linear or log-log axis scales in the literature. It was proposed by Gu *et al.* [48] that the dependence should follow qualitatively the steady-state Dember-voltage expression given by Eq. (4), and we find that our results are in line with this hypothesis.

For a given pump wavelength, three distinct regions are identified, as seen in Fig. 4. At a high power, the amplitude becomes independent of the pulse energy, and one possibility is that photogenerated carriers in the first half of the pulse induce a Coulomb repulsion on those of the second half [12]. This saturation is not included in the model, so the calculated curves do not match the data points. Below this range is a large portion where the amplitude varies with the logarithm of the energy per pulse, as predicted by Eq. (4), and also with the time-dependent simulations, as shown in the figure. In this regime, as the number of photons increases, more electrons are available to participate in the radiation process, but this change is moderated by the increased Coulomb attraction to the holes. However, this effect is not saturation but rather an intrinsic part of the photo-Dember mechanism. Finally, at a low enough carrier concentration, electrons are free to accelerate as the Coulomb attraction gets weaker, and the radiation is more or less proportional to the number of generated electrons. This last portion is also predicted by the calculation and is observed experimentally.

The transition between the linear and logarithmic dependencies varies with the pump wavelength. If more kinetic energy is given to each electron, a higher density is required for the Coulomb attraction to be effective in slowing them down. In the case of a continuous excitation,

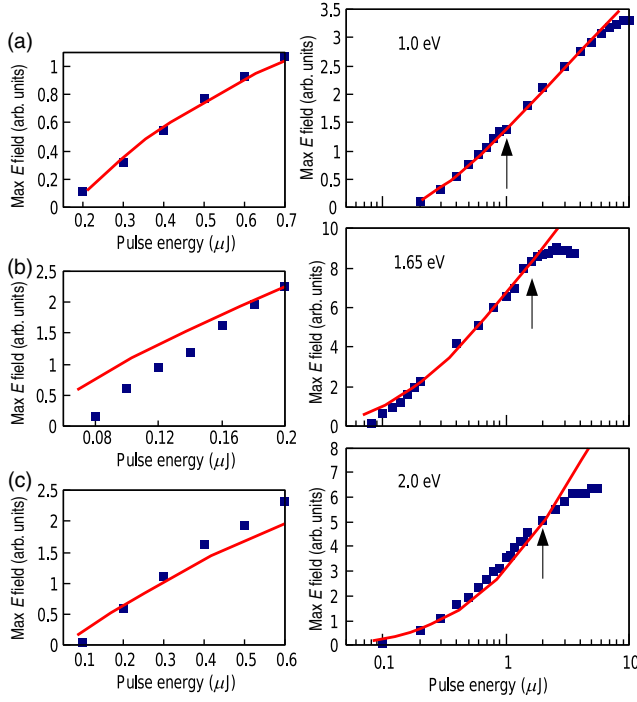


FIG. 4. (a) Dependence of the terahertz emission maximum amplitude as a function of the energy per pulse at 1.0 eV for InAs. The left and right plots use linear and logarithmic scales, respectively, for the x axis. The y axis has a linear scale in both graphs. Data points and lines show experimental and calculated values, respectively. (b),(c) Plots with the same arrangement at 1.65 and 2.0 eV, respectively. Arrows show the energy per pulse used in Fig. 2. In the calculated curves, adjusted scaling factors of 0.6, 1.0, and 0.9 have been used in (a), (b), and (c), respectively, which is within the experimental precision of Fig. 2.

the background carrier concentration determines the linear-to-logarithmic dependence transition region [Eq. (4)]. In the time-dependent calculation, the mechanism is slightly different and cannot be described with a single equation, and the transition occurs at densities around 10^{17} cm^{-3} , which is larger than the background carrier concentration. The simulated and measured data in Fig. 4 are in excellent agreement, which is a convincing argument for the validity of the model. The arrows in Fig. 4 show the energy per pulse used for the measurements of Figs. 1 and 2, which are always below the saturation region.

B. GaAs and InSb analysis

A second consistency check comes from the analysis of GaAs and InSb samples, performed under the same excitation conditions below saturation with a constant number of photons. GaAs has a band configuration similar to InAs, but a larger fundamental gap. Figure 5(a) shows a detailed curve fit at 2.0 eV. The valley before the maximum amplitude is deeper than for InAs, a feature that we attribute to a larger surface band bending. The model reproduces well the main peak and the following

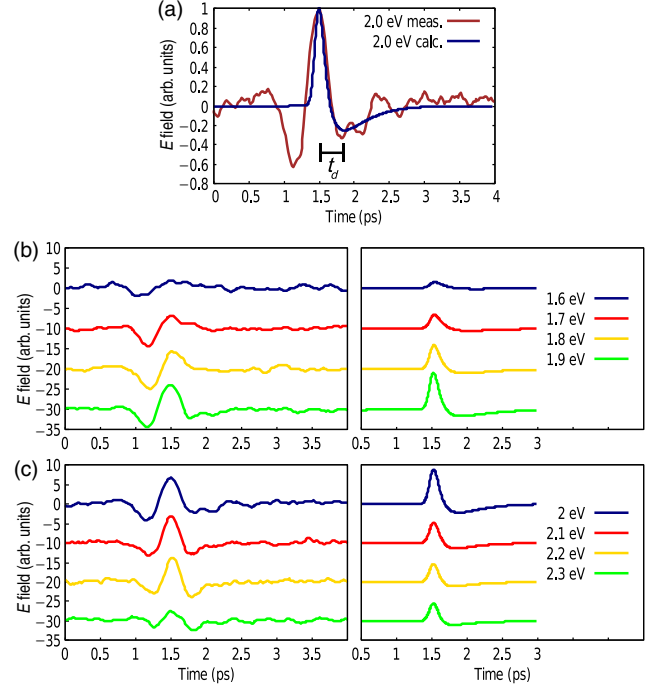


FIG. 5. (a) Overlapped experimental and simulated GaAs terahertz emission curves in the time domain at 2.0 eV, i.e., in the vicinity of the maximum signal. (b) Experimental (left panel) and simulated (right panel) terahertz emission curves for a signal strength that increases with the photon energy. (c) Experimental (left panel) and simulated (right panel) terahertz emission curves for a signal strength that decreases with the photon energy. Electron-hole energy equilibrium is assumed for the calculations. The horizontal position of the curves is adjusted to obtain a peak at 1.5 ps.

valley. Both experimentally and numerically, using the same broadening parameter values as for InAs, the time delay t_d between the maximum and the minimum is 0.35 ps, which is 50 fs longer than for InAs. The difference is explained by the lower carrier mobility in GaAs and by the different Γ electron-to-hole mobility ratio, which is around 100 for InAs and 30 for GaAs at low energy. In Fig. 5(c), the valley minimum is deeper in the experimental and simulated curves, a fact that is again attributed to the L -valley scattering slowing down carriers more efficiently.

Figure 6(a) shows the dependence of the maximum signal as a function of the pump wavelength. The range below 1.6 eV with a nonregular variation is attributed to the built-in electric field and is not discussed further. Between approximately 1.6 and 1.95 eV, a linearly rising signal is observed due to the increasing carrier kinetic energy, followed by a transition to a more or less flat dependency in the 2–2.2 eV range and a linear decrease at higher energy. Figure 6(b) shows the simulated plot for equal hole-electron momenta (yellow) and for equal kinetic energies (blue), and we observe again that the latter curve

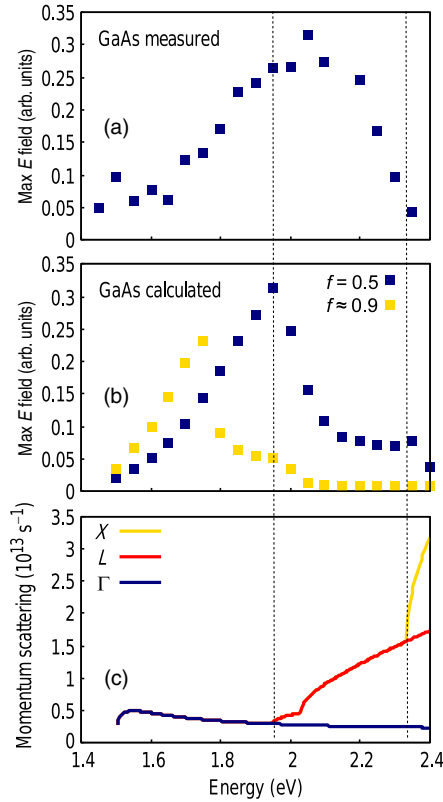


FIG. 6. (a) Plot of the maximum experimental time-domain terahertz signal for GaAs as a function of the pump wavelength. (b) Simulated result with equal hole and Γ -electron kinetic energy (blue) and equal momentum (yellow). (c) Calculated Γ -band scattering rate for equal kinetic energy. The legend refers to the band to which carriers are scattered. The dashed lines positioned at the phonon-absorption thresholds show the alignment of features in (a), (b), and (c).

with $f = 0.5$ allows us to positively associate the end of the linear signal increase with the onset of scattering to the L valley. For the L -valley effective mass, we use a value $m_L = 0.2m_0$, which is between the longitudinal and transverse published data. At a higher energy, we find a sharper decrease in the simulated curve, a fact that we attribute to a roll-off effect in the measured result due to the finite carrier energy distribution. With a nonadjusted value $m_X = 0.8m_0$ of the X -valley effective mass, we obtain overall a dependency that is reasonably similar to the experimental results and a clear correlation with the Γ -valley electron momentum scattering shown in Fig. 6(c) for $f = 0.5$.

Overall, we notice that the transition corresponding to the onset of upper-valley scattering is not as well defined for GaAs as for InAs, a plateau as opposed to a peak. Such behavior is not surprising if one considers the lower carrier mobility that could lead to a wider carrier energy distribution in GaAs, as well as a lower experimental signal strength, leading to slightly more scattered data points. Some remaining effect of a surface built-in field due to the

larger band gap may also be involved, as well as the influence of the different scattering thresholds for phonon absorption and emission as seen in Fig. 6(c). In the vicinity of the L -valley scattering threshold, the signal amplitude results from the balance of a number of factors, which may lead to rounded-off features.

InSb has a band configuration that is different, as the X valley lies only 395 meV above the Γ band and is below the L valley. Moreover, the energy difference between the top of the heavy hole and the split-off bands is 800 meV, compared to 410 and 340 meV for InAs and GaAs, respectively [43]. An examination of the experimental terahertz curve obtained in the vicinity of the maximum signal, as shown in Fig. 7(a), reveals that the time delay between the main peak and the following valley t_d is larger, around 0.5 ps. While the reason for this observation cannot be confirmed beyond any doubt, we discuss the possibility that it could be explained by an optical-alignment effect of the carrier momentum [22] due to the band structure. Based on symmetry rules for a zinc-blende crystal, electrons excited from the heavy-hole and light-hole bands have their momentum-distribution maxima oriented perpendicular and parallel to the light polarization vector,

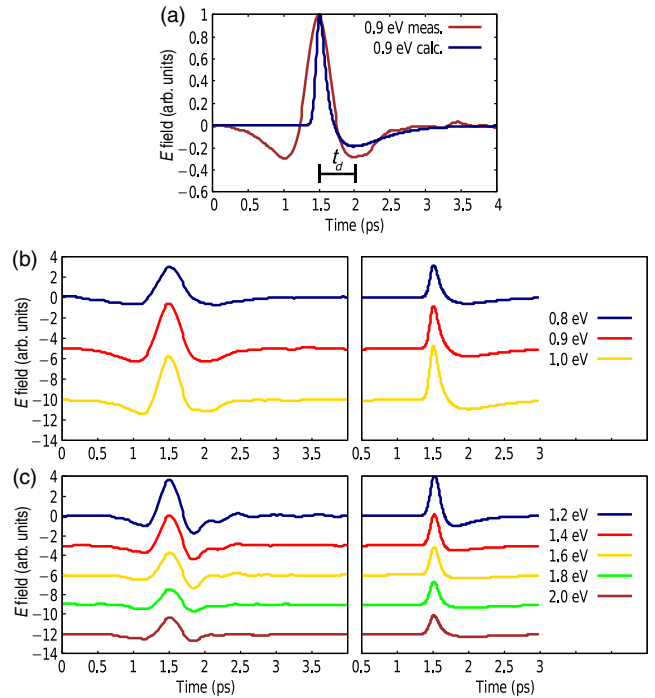


FIG. 7. (a) Overlapped experimental and simulated InSb terahertz emission curves in the time domain at 0.9 eV, i.e., in the vicinity of the maximum signal. (b) Experimental (left panel) and simulated (right panel) terahertz emission curves for a signal strength that increases with the photon energy. (c) Experimental (left panel) and simulated (right panel) terahertz emission curves for a signal strength that is decreasing or constant with the photon energy. Electron-hole energy equilibrium is assumed for the calculations. The horizontal position of the curves is adjusted to obtain a peak at 1.5 ps.

respectively, while there is no preferred orientation for the split-off band [49]. Electrons originating from the light-hole band initially have a low velocity along the propagation axis, which would slow down the diffusion process. For InSb only, for a photon energy in the vicinity of the emission amplitude maximum, carriers are excited far from the split-off band. The light- to heavy-hole transition probability ratio is 1:3 [50]. For InAs and GaAs, on the other hand, transitions also involving the split-off band are possible [51].

For the simulation, in Eq. (14), we decrease the initial carrier velocity v_z in the Γ band to 75% of its maximum at a time corresponding to the center of the light pulse and introduce a relaxation time to the full velocity (the isotropic momentum) equal to $\tau_m/5 \approx 0.2$ ps. This second broadening mechanism is in line with an optical-alignment phenomenon, as described in the previous paragraph, and gives an excellent match to the experimental curve valley position, as shown in Fig. 7(a). When the momentum scattering rate increases due to the contribution of the X and L bands, this effect is not observable, as carriers undergo more collisions (a smaller τ_m) and the valley position returns to a value $t_d \approx 0.3$ ps, similar to InAs. This variation is seen in both the experimental and simulated curves of Figs. 7(b) and 7(c). In the frequency domain, this shift is also observable, with a peak located in the 0.6–0.7 THz range and near 1 THz below and above 1.0 eV, respectively.

A plot of the maximum signal as a function of the excitation wavelength, as shown in Fig. 8(a), reveals some interesting features, as the influence of both the X and L valleys can be probed. In addition to the monotonic signal increase up to 1.0 eV and the following threshold associated with the X -valley bottom, the plateau region near 1.8–2.0 eV can be positively associated with the onset of the L -valley scattering for equal electron and hole energies, as seen by a comparison to Fig. 8(c). While there is no established experimental value for the X - and L -valley effective masses in the literature, it is expected from theoretical calculations that m_X will be larger than m_L [52]. We observe a slope of a smaller magnitude in the 2.0–2.4 eV range than in the 1.2–1.6 eV range, which could be related to this fact. For the simulation shown in Fig. 8(b), we obtain a reasonable fit by using the realistic values (which are comparable to InAs) $m_X = 0.1m_0$ and $m_L = 0.09m_0$. A sharper decrease in the 1.0–1.2 eV range is observed in the calculated result, which we attribute again to a rollover effect related to the finite electron energy distribution not being taken into account. In the calculated curve, a kink is found at 1.5 eV that is due to an increase of the photon absorption coefficient and of the diffusion current. This feature, obtained with the standard refractive-index values used, is not observed experimentally and could be washed out by the large free-carrier concentration.

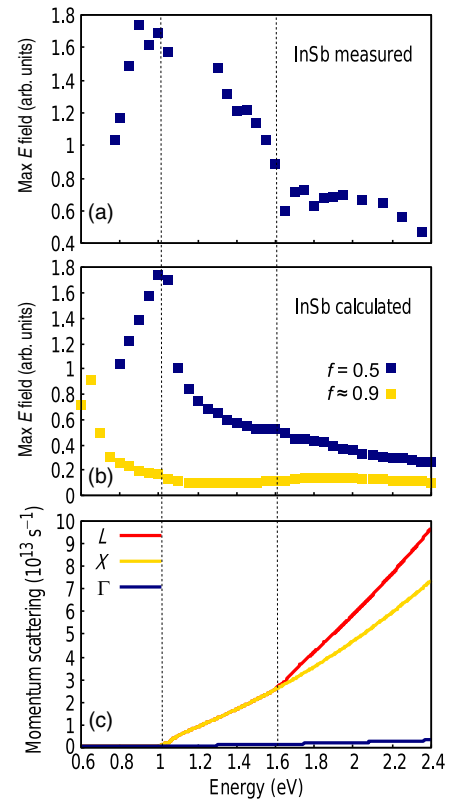


FIG. 8. (a) Plot of the experimental maximum time-domain terahertz signal for InSb as a function of the pump wavelength. (b) Simulated result with equal hole and Γ -electron kinetic energy (blue) and equal momentum (yellow). (c) Calculated Γ -band scattering rate for equal kinetic energy. The legend refers to the band to which carriers are scattered. Dashed lines positioned at the phonon-absorption thresholds show the correlation of features in (a), (b), and (c).

V. SUMMARY AND OUTLOOK

In this work, we attempt to illustrate the potential of the development of simulation environments intrinsically taking into account Coulomb forces beyond a quasistatic Poisson approximation for the description of electron-hole plasma dynamics. There is a trend towards the realization of compact, higher-density structures including UV-visible integrated photonics and a need to investigate the fundamental limits involved. The related numerical applications may not be restricted to this experimental work and may extend to other devices with a relatively high carrier density, such as ultrafast pulsed semiconductor lasers or p - i - n diodes for high-power electronics.

We show that rich information can be gathered from terahertz emission experiments by considering the peak signal amplitude. Upon photoexcitation, electron and hole carriers reach a rapid thermal equilibrium, and the maximum of the diffusion- and conduction-current components occurs at a time close to the peak of the optical pulse. Depending on the photon energy, the electron transfer to upper valleys is completed within a delay of around 0.1 to

1.0 ps following excitation, as shown in Fig. 3. In a comparable time, the Demer field reaches a maximum value at a position in the vicinity of the carrier penetration depth in the material if recombination effects are small. The amplitude dependence on the photon energy (the excitation wavelength) can be explained by considering a balance of several factors, as the signal increases for a larger electron kinetic energy and photon-absorption coefficient, but decreases with a larger hole kinetic energy and smaller electron population and momentum scattering time in the Γ valley. For a given excitation wavelength, the dependence of the emission amplitude below saturation varies with the logarithm of the energy per pulse as the effect of the increasing number of accelerating electrons is tempered by the stronger electron-hole attraction.

As the features that we obtain are sharp, a measurement that could be performed next would be a scan of the excitation wavelength for a number of photons per pulse of a smaller order of magnitude to find if a region in which the electrons and holes have different temperatures (equal electron-hole momentum, $f \approx 0.9$) could be detected. The results that we have described tend to indicate that it would be possible with a quasi-one-dimensional approximation to obtain a quantitative picture of photoexcited carrier motion that is complete to an extent similar to that reached with unipolar devices. The inclusion of other effects in the present numerical model with fixed energy, such as an applied or built-in electric field or partial reflection or absorption at the surface or at a given depth, could be considered for structures including thin layers. For a more accurate reproduction of the shape of the experimental curves shown in Figs. 6(a) and 8(a) in the regions where the L and X valleys participate in the process, a simulation with finite photon and carrier energy distributions could be developed.

The experimental graphs in the time domain seen in Figs. 1, 5, and 7 have stable features, even with different samples over a wide range of photon energy, with a main peak preceded and followed by valleys. While we comment on the position of the second valley in this work by including a phenomenological broadening term, a more accurate reproduction of these curves would require further analysis, the first step being the deconvolution of the response of the detection system. The effect of optical alignment involving the valence bands, variation within the pulse area, and other factors could next be considered and a two- or three-dimensional calculation may be advantageous.

A model including the saturated regime observed in Fig. 4 would also be useful for bridging the gap to a higher fluence and may be relevant for a better understanding of light wavelength dependence of various laser-processing applications, as well as saturation effects in devices. Furthermore, coupled experimental and numerical studies of carrier dynamics in complex materials including polycrystals and quantum wires would be of interest. Finally, a

multidimensional analysis would definitely be required for the study of magnetically ordered samples, as the original motivation for this work was our previous observation that terahertz emission is very sensitive to spin orientation in ferromagnetic (Ga,Mn)As [53], in which carriers undergo a pronounced direction change.

ACKNOWLEDGMENTS

This work was supported by JSPS KAKENHI Grants No. 15104006 and No. 26247049 (M. K.-G.). The authors would like to thank Dr. K. Konishi for the useful discussions. J. B. H. would like to thank Professor J. F. Bisson for the useful discussions.

-
- [1] N. Dupuis, D. M. Kuchta, F. E. Doany, A. Rylyakov, J. Proesel, C. W. Baks, C. L. Schow, S. Luong, C. Xie, L. Wang, S. Huang, K. Jackson, and N. Y. Li, in *Proceedings of the 2014 Optical Fiber Communications Conference and Exhibition (OFC), San Francisco, 2014* (OSA Publishing, Washington, DC, 2014), p. M3G.5, <https://doi.org/10.1364/OFC.2014.M3G.5>.
 - [2] J. W. Shi, K. L. Chi, C. Y. Li, and J. M. Wun, Dynamic analysis of high-efficiency InP-based photodiode for 40 Gbit/s optical interconnect across a wide optical window (0.85 to 1.55 μm), *J. Lightwave Technol.* **33**, 921 (2015).
 - [3] L. Shen, E. Y. B. Pun, and J. C. Ho, Recent developments in III-V semiconducting nanowires for high-performance photodetectors, *Mater. Chem. Front.* **1**, 630 (2017).
 - [4] X. Dai, S. Zhang, Z. Wang, G. Adamo, H. Liu, Y. Huang, C. Couteau, and C. Soci, GaAs/AlGaAs nanowire photodetector, *Nano Lett.* **14**, 2688 (2014).
 - [5] See, e.g., O. Gref, A. M. Teodoreanu, R. Leihkauf, H. Lohrke, M. Kittler, D. Amkreutz, C. Boit, and F. Friedrich, Grain boundary light beam induced current: A characterization of bonded silicon wafers and polycrystalline silicon thin films for diffusion length extraction, *Phys. Status Solidi A* **213**, 1728 (2016); J. Bauer, F. Fruhauf, and O. Breitenstein, Quantitative local current-voltage analysis and calculation of performance parameters of single solar cells in modules, *Sol. Energy Mater. Sol. Cells* **159**, 8 (2017).
 - [6] See, e.g., O. Schubert, M. Hohenleutner, F. Langer, B. Urbanek, C. Lange, U. Huttner, D. Golde, T. Meier, M. Kira, S. W. Koch, and R. Huber, Sub-cycle control of terahertz high-harmonic generation by dynamical Bloch oscillations, *Nat. Photonics* **8**, 119 (2014).
 - [7] L. J. Bond, Needs and opportunities: nondestructive evaluation for energy systems, *Proc. SPIE Int. Soc. Opt. Eng.* **9439**, 943902 (2015).
 - [8] I. Nevinskas, S. Stanionyte, V. Pacebutas, and A. Krotkus, Terahertz emission from GaInAs *p-i-n* diodes photoexcited by femtosecond laser pulses, *Lith. J. Phys.* **55**, 274 (2015).
 - [9] V. N. Trukhin, A. S. Buyskikh, N. A. Kaliteevskaya, A. D. Bouraulev, L. L. Samoilov, Yu. B. Samsonenko, G. E. Cirilin, M. A. Kaliteevski, and A. J. Gallant, Terahertz generation by GaAs nanowires, *Appl. Phys. Lett.* **103**, 072108 (2013).

- [10] K. A. Salek, H. Nakanishi, A. Ito, I. Kawayama, H. Murakami, and M. Tonouchi, Laser terahertz emission microscopy studies of a polysilicon solar cell under the illumination of continuous laser light, *Opt. Eng. (Bellingham, Wash.)* **53**, 031204 (2014).
- [11] H. Dember, Photoelectric E.M.F. in cuprous-oxide crystals, *Phys. Z.* **32**, 554 (1931).
- [12] Ping Gu and Masahiko Tani, in *Terahertz Optoelectronics*, edited by K. Sakai (Springer, Berlin, 2005), Chap. 4, p. 63.
- [13] X.-C. Zhang and D. H. Auston, Optoelectronic measurement of semiconductor surfaces and interfaces with femtosecond optics, *J. Appl. Phys.* **71**, 326 (1992).
- [14] J. N. Heyman, N. Coates, A. Reinhardt, and G. Strasser, Diffusion and drift in terahertz emission at GaAs surfaces, *Appl. Phys. Lett.* **83**, 5476 (2003).
- [15] M. Reid and R. Fedosejevs, Terahertz emission from (100) InAs surfaces at high excitation fluences, *Appl. Phys. Lett.* **86**, 011906 (2005).
- [16] G. D. Chern, E. D. Readinger, H. Shen, M. Wraback, C. S. Gallinat, G. Koblmüller, and J. S. Speck, Excitation wavelength dependence of terahertz emission from InN and InAs, *Appl. Phys. Lett.* **89**, 141115 (2006).
- [17] K. Liu, J. Xu, T. Yuan, and X.-C. Zhang, Terahertz radiation from InAs induced by carrier diffusion and drift, *Phys. Rev. B* **73**, 155330 (2006).
- [18] M. Suzuki, M. Tonouchi, K.-I. Fujii, H. Ohtake, and T. Hirosumi, Excitation wavelength dependence of terahertz emission from semiconductor surfaces, *Appl. Phys. Lett.* **89**, 091111 (2006).
- [19] L. Liu, Z. Zheng, X. Zhao, S. Sun, J. Liu, and J. Zhu, Experimental comparison of characteristics of magnetic-field-enhanced InAs and InSb Dember terahertz emitters pumped at 1550 nm wavelength, *J. Opt. A* **14**, 045204 (2012).
- [20] R. Adomavicius, G. Molis, A. Krotkus, and V. Sirutkaitis, Spectral dependencies of terahertz emission from InAs and InSb, *Appl. Phys. Lett.* **87**, 261101 (2005).
- [21] G. Molis, A. Krotkus, and V. Vaicai, Intervalley separation in the conduction band of InGaAs measured by terahertz excitation spectroscopy, *Appl. Phys. Lett.* **94**, 091104 (2009).
- [22] A. Arlauskas and A. P. Krotkus, THz excitation spectra of AIII BV semiconductors, *Semicond. Sci. Technol.* **27**, 115015 (2012).
- [23] M. Tonouchi, N. Uchida, S. Kim, R. Inoue, and H. Murakami, Laser terahertz emission microscope, *Terahertz Sci. Technol.* **1**, 28 (2008).
- [24] H. Nakanishi, A. Ito, K. Takayama, I. Kawayama, H. Murakami, and M. Tonouchi, Comparison between laser terahertz emission microscope and conventional methods for analysis of polycrystalline silicon solar cell, *AIP Adv.* **5**, 117129 (2015).
- [25] K. A. Salek, I. Kawayama, H. Murakami, and M. Tonouchi, Evaluation of solar cell using terahertz time-domain spectroscopy, *Phys. Sci. Int. J.* **6**, 96 (2015).
- [26] M. B. Johnston, D. M. Whittaker, A. Corchia, A. G. Davies, and E. H. Linfield, Simulation of terahertz generation at semiconductor surfaces, *Phys. Rev. B* **65**, 165301 (2002).
- [27] M. Abe, S. Madhavi, Y. Shimada, Y. Otsuka, K. Hirakawa, and K. Tomizawa, Transient carrier velocities in bulk GaAs: Quantitative comparison between terahertz data and ensemble Monte Carlo calculations, *Appl. Phys. Lett.* **81**, 679 (2002).
- [28] K. J. Chau and A. Y. Elezabi, Two-dimensional drift-diffusion analysis of magnetic field enhanced THz emission from semiconductor surfaces, *Opt. Commun.* **242**, 295 (2004).
- [29] V. L. Malevich, Monte Carlo simulation of the Dember effect in *n*-InAs exposed to femtosecond pulse laser excitation, *Semiconductors* **40**, 155 (2006).
- [30] Dong-Feng Liu and Du Xu, Comparative study of terahertz radiation from *n*-InAs and *n*-GaAs, *Appl. Opt.* **46**, 789 (2007).
- [31] V. M. Polyakov and F. Schwierz, Influence of band structure and intrinsic carrier concentration on the THz surface emission from InN and InAs, *Semicond. Sci. Technol.* **22**, 1016 (2007).
- [32] A. Reklaitis, Terahertz emission from InAs induced by photo-Dember effect: Hydrodynamic analysis and Monte Carlo simulations, *J. Appl. Phys.* **108**, 053102 (2010).
- [33] D. L. Cortie and R. A. Lewis, Role of vanguard counter-potential in terahertz emission due to surface currents explicated by three-dimensional ensemble Monte Carlo simulation, *Phys. Rev. B* **84**, 155328 (2011).
- [34] K. Tomizawa, *Numerical Simulation of Submicron Semiconductor Devices* (Artech House, Boston, 1993).
- [35] E. Kojima, J. B. Héroux, R. Shimano, Y. Hashimoto, S. Katsumoto, Y. Iye, and M. Kuwata-Gonokami, Experimental investigation of polaron effects in Ga_{1-x}Mn_xAs by time-resolved and continuous-wave midinfrared spectroscopy, *Phys. Rev. B* **76**, 195323 (2007).
- [36] B. Hwang and F. A. Lindholm, Dember effect in fast photoconductive circuit elements, *IEEE Trans. Electron Devices* **31**, 101 (1984).
- [37] B. Hwang and F. A. Lindholm, Transient establishment of the Dember field in fast photoconductive circuit elements, *IEEE Trans. Electron Devices* **32**, 2378 (1985).
- [38] J. Shan and T. F. Heinz, Terahertz radiation from semiconductors, *Top. Appl. Phys.* **92**, 1 (2004).
- [39] Winfried Monch, *Semiconductor Surfaces and Interface: Surfaces Sciences* (Springer, Berlin, 1993), p. 68.
- [40] J. S. Blakemore, Semiconducting and other major properties of gallium arsenide, *J. Appl. Phys.* **53**, R123 (1982).
- [41] Mark Lundstrom, *Fundamentals of Carrier Transport*, 2nd ed. (Cambridge University Press, Cambridge, England, 2000).
- [42] I. Vurgaftman, J. R. Meyer, and L. R. Ram-Mohan, Band parameters for III-V compounds and their alloys, *J. Appl. Phys.* **89**, 5815 (2001).
- [43] Electronic archive: New semiconductor materials characteristics and properties, www.ioffe.ru/SVA/NSM/Semicond/.
- [44] E. D. Palik, *Handbook of Optical Constants of Solids* (Academic Press, New York, 1985).
- [45] M. V. Fischetti, Monte Carlo simulation of transport in technologically significant semiconductors of the diamond and zinc-blende structures—Part I: Homogeneous transport, *IEEE Trans. Electron Devices* **38**, 634 (1991).
- [46] S. Asmontas, R. Raguotis, and S. Bumelien, Monte Carlo study of impact ionization in InSb induced by intense ultrashort terahertz pulses, *Appl. Phys. A* **120**, 1241 (2015).

- [47] Jagdeep Shah, *Ultrafast Spectroscopy of Semiconductors and Semiconductor Nanostructures* (Springer, New York, 1986).
- [48] P. Gu, M. Tani, S. Kono, K. Sakai, and X.-C. Zhang, Study of terahertz radiation from InAs and InSb, *J. Appl. Phys.* **91**, 5533 (2002).
- [49] D. N. Mirlin, in *Optical Orientation*, Modern Problems in Condensed Matter Sciences Vol. 8, edited by F. Meier and B. P. Zakharchenya (Elsevier, New York, 1984), Chap. 4, p. 133.
- [50] Gerald Bastard, *Wave Mechanics Applied to Semiconductor Heterostructures* (Halsted Press, New York, 1988), p. 247.
- [51] Mark Fox, *Optical Properties of Solids* (Oxford University Press, Oxford, 2001), p. 57.
- [52] Z. G. Zhu, T. Low, M. F. Li, W. J. Fan, P. Bai, D. L. Kwong, and G. Samudra, Pseudo-potential band structure calculation of InSb ultra-thin films and its application to assess the *n*-metal-oxide-semiconductor transistor performance, *Semicond. Sci. Technol.* **23**, 025009 (2008).
- [53] J. B. Héroux, Y. Ino, M. Kuwata-Gonokami, Y. Hashimoto, and S. Katsumoto, Terahertz radiation emission from GaMnAs, *Appl. Phys. Lett.* **88**, 221110 (2006).